International Journal of Nanoelectronics and Materials
IJNeaM
ISSN 1985-5761 | E-ISSN 2232-1535

The Effects of Temperature on CO_2 Corrosion of Mild Steel in 3.5 wt.% NaCl: Corrosion Rate, Surface Morphology, and Phase Characterisation

Engku Sofiyyah Hanan Engku Omar Amiruddin[a], Norinsan Kamil Othman[a,*], Rabiahtul Zulkafli[b], Vincent Onuegbu Izionworu[c], and Wan Mohd Norsani Wan Nik[d]

[a]*Department of Applied Physics, Faculty of Science and Technology, Universiti Kebangsaan Malaysia, 43600 Bangi, Selangor, Malaysia*
[b]*Department of Earth Science and Environment, Faculty of Science and Technology, Universiti Kebangsaan Malaysia, 43600 Bangi, Selangor, Malaysia*
[c]*Department of Chemical/Petrochemical Engineering, Rivers State University, Nkpolu-Oroworukwo, Port Harcourt, Nigeria*
[d]*Department of Maritime Technology, Faculty of Maritime Studies and Marine Science, Universiti Malaysia Terengganu, 21030 Kuala Nerus, Terengganu*
* *Corresponding author. Tel.: +6017-6834050; e-mail: insan@ukm.edu.my*

Received 15 September 2023, Revised 1 October 2025, Accepted 27 October 2025

ABSTRACT

CO_2 corrosion of mild steel constitutes a significant integrity threat within hydrocarbon transport systems. This work comparatively investigates the temperature-dependent corrosion behaviour of mild steel in CO_2-saturated and CO_2-free environments through weight loss test, surface morphology, and phase characterisation. Mild steel samples were exposed to two media, which are CO_2-rich 3.5% NaCl solution and CO_2-free 3.5% NaCl solution at 25°C, 40°C, 60°C, and 80°C for 7 days. Morphology changes, microstructure of corrosion products, cross sections, and phase characterisation were analysed using field emission scanning electron microscopy (FESEM), optical microscope (OM), and X-ray diffraction (XRD). Results from weight loss tests found that an increase in temperature resulted in an accelerated corrosion rate. However, in a CO_2 environment, a decrease in corrosion rate was observed at higher temperatures, attributed to the emergence of protective layers. FESEM images revealed that mild steel in a CO_2 environment underwent uniform corrosion, whereas localised corrosion was observed in the absence of CO_2. The corrosion scales thickened with increasing temperature in both media; however, the development of a protective carbonate layer in the CO_2 environment inhibited further deposition, leading to a thinner final layer. XRD analysis confirmed the formation of siderite, hematite, and ferrous hydroxide in a CO_2 environment, while cementite, hematite, and ferric oxyhydroxide were identified in a non-CO_2 environment. These findings suggest that while temperature initially accelerates sweet corrosion, the emergence of a compact $FeCO_3$ scale above 60°C transitions the behaviour to partial protection, guiding the developing temperature-dependent mitigation strategies and the application of nano-enabled monitoring in CO_2-rich pipeline environments.

Keywords: *AISI 1015 mild steel, CO_2 corrosion, NaCl solution, siderite, temperature*

1. INTRODUCTION

The pipeline structure in the petroleum and gas refining and transportation industries often experiences failure due to corrosion problems. In the natural gas sector, mild steel remains the predominant material for oil and gas equipment and fabrication, such as ASTM A105 carbon steel flanges in bolted joints and ASTM A516 Gr.70 pressure vessel plate in tanks or vessels, owing to its favourable mechanical properties and economic viability [1]–[3] Studies report low carbon API 5L grades ($C \leq 0.26$ wt.%, $Mn \approx 0.5\text{-}1.6$ wt.%) such as X42, X52, X60, X65, and X80 are the most commonly used for pipeline steel grades in oil and gas transportation [4], [5] However, pipeline structure corrosion is significantly influenced by environmental parameters, including temperature, pH, and salinity. The presence of aggressive constituents, including free water, carbon dioxide (CO_2), and hydrogen sulphide (H_2S) in natural gas and crude oil, poses a significant risk to the integrity of carbon steel infrastructure. Under these conditions, the interior surfaces of oil and gas pipes are very susceptible to corrosion damage [6]

Corrosion is a natural phenomenon that occurs when steel reacts with its environment to form a more stable compound. In the oil and gas industry, extensive research has been done to understand CO_2 corrosion, also referred to as sweet corrosion, resulted in various theories and mechanistic interpretations over the years [7] The corrosion of carbon steel due to dissolved CO_2 poses a significant threat to the oil and gas industry [8] A study by the Malaysia Natural Gas Industry Annual Review in 2017 reported that Malaysia is facing a critical issue related to the high presence of CO_2 gas during gas extraction processes [9] The complexity of corrosion processes in CO_2-rich saline solutions arises from the combined effects of environmental conditions, physical parameters, and metallurgical characteristics of the steel [10] Therefore, understanding the environmental factors influencing CO_2 corrosion mechanisms is important to develop effective mitigation strategies.

In the oil and gas sector, carbon steel components commonly operate within a temperature range from ambient to 425°C [11] CO_2 corrosion is significantly influenced by thermal conditions [10] Generally, elevated temperature enhances the mass transfer and electrochemical kinetics, thereby accelerating the corrosion process. The corrosion behaviour of C1010 and C1018 carbon steels was investigated in CO_2-saturated environments across 25–80 °C and 0.001–10 wt.% NaCl, reporting an elevated corrosion rate during the early immersion phase [8] However, a decline in corrosion rate was observed at 60°C and 80°C due to the rapid growth of a protective $FeCO_3$ layer. Another finding also reported that the highest CO_2 corrosion rates occur within the temperature range of 60°C–90°C [12]

Despite CO_2 corrosion being widely investigated, the understanding of the phenomenon remains limited due to its complexity and the significant impact of environmental factors on the corrosion product formation [13] In this study, the impact of temperature on the sweet corrosion behaviour of AISI 1015 steel in 3.5% NaCl solution was examined. The goal was to improve understanding of the impact of thermal conditions on CO_2 corrosion mechanisms. Tests were performed on AISI 1015 carbon steel as a compositionally simple mild steel baseline. This enables us to attribute corrosion rate changes primarily to environmental parameters such as temperature, pH, and the presence of CO_2 rather than to microalloying effects. Weight loss test, morphological changes, cross-sectional analysis, and corrosion product phases were conducted to understand the corrosion behaviour.

2. MATERIALS AND METHODS

2.1. Sample Preparation

SAE/AISI 1015 grade mild carbon steel obtained from a local supplier in Jenaris, Kajang, Selangor, was used in this study. AISI 1015 was selected because its minimal alloying and ferrite–pearlite microstructure make it an appropriate baseline for attributing corrosion rate changes primarily to temperature and solution chemistry rather than microalloying effects. Table 1 outlines the elemental composition of the AISI 1015 mild steel used in this study. The sample was cut to dimensions of 20 mm × 20 mm × 2 mm, and a small hole with a diameter of 1.5 mm was drilled as shown in Figure 1. The hole was made to allow the sample to be suspended during the corrosion test. The sample was then ground using a disc grinder with silicon carbide paper starting from grit 60, 240, 320, 600, 800, 1000, and 1200 to remove impurities and oxide layers that would interfere with experimental results. At each grinding stage, the sample was cleaned using Teepol soap and rinsed with distilled water. The sample was dried using a hot air dryer and stored properly in a container with silica gel. The container was placed in a dry box to prevent any unwanted reaction between the sample and the environment.

Table 1 Chemical composition of mild carbon steel AISI 1015 in (wt.%)

Element	C	Mn	P	S	Fe
Composition (wt.%)	0.15	0.40	0.02	0.03	99.40

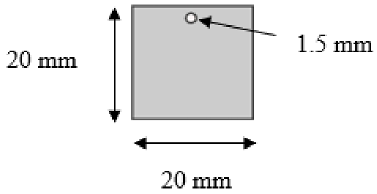

Figure 1. Mild steel sample dimensions.

2.2. Media Preparation

An electrolyte of 3.5 wt.% sodium chloride (NaCl) was selected as a seawater salinity surrogate, reflecting field-relevant marine exposure while keeping the matrix simple for isolating temperature and CO_2-dependent corrosion mechanisms [14] The electrolyte is prepared following ASTM D1141-98, where 35 g of analytical-grade NaCl (≥99.5%, Sigma-Aldrich, USA) is dissolved in ~900 mL of distilled water and then bringing the mixture to a final mass of 1000 g at 25 ± 0.5°C. The initial pH of the solution ranged between 6.4 and 7.2. Corrosion experiments were conducted under two conditions, which were with and without CO_2 gas saturation. Two separate glass cells, each containing the NaCl solution, were used for the respective environments. Both cells were maintained at constant temperature using a water bath system. Mild steel specimens were suspended using nylon threads to ensure full immersion in the solution without contact with the beaker base. The immersion period was fixed at seven days for each test. Corrosion tests were performed at 40°C, 60°C, and 80°C to reflect common pipeline operating conditions and to span the field-observed transition from active dissolution to formation of protective $FeCO_3$ film [15]–[17] The experimental setup and immersion procedure were conducted in accordance with ASTM G31, which recommends a 7-day exposure duration for corrosion testing to ensure a robust and consistent formation of corrosion products [18] Control specimens were immersed in CO_2-saturated and CO_2-free 3.5% NaCl solutions at ambient temperature (25 °C) for seven days to serve as reference benchmarks. For each condition, two independent replicates were performed (n = 2) owing to limited experimental throughput within the one-year project timeline, and the results are reported as mean ± SD.

2.3. pH Measurement

pH was measured using a handheld meter (Thermo Scientific Eutech pH 150). pH was monitored daily for seven consecutive days (t = 0 and at ~24 h intervals through Day 7) for both electrolytes. Before each measurement session, the glass electrode was rinsed with distilled water and calibrated by two-point calibration with NIST traceable buffer solutions (pH 4.01 and 7.00, 25 °C). The probe was first immersed in the pH 4.01 buffer to complete the first calibration point, rinsed with distilled water, and then calibrated in the pH 7.00 buffer. After calibration, the electrode was rinsed with distilled water and immediately immersed in the electrolyte for measurement (both the CO_2-saturated and CO_2-free 3.5 wt% NaCl solutions). Readings were recorded once stable, and the electrode was rinsed with distilled water between measurements.

2.4. Corrosion Rate

Weight loss measurements were used to determine the corrosion rate following the guidelines specified in ASTM G31 [18] Corrosion scale was removed by following the ASTM G1-03 standard to ensure accurate measurement of the specimen's final mass [19] The mass of each specimen was recorded before and after immersion using an analytical balance. The corrosion rate (CR), expressed in millimeters per year (mm/y), was determined using the following formula:

$$CR = \frac{K \cdot W}{A \cdot t \cdot \rho} \tag{1}$$

where K is constant (8.76×10^4), W represents the weight loss in grams (g), A denotes the exposed surface area of the specimen in square centimeters (cm^2), t is the immersion time in hours (h), and ρ is the material density (7.85 g/cm^3).

2.5. Field Emission Scanning Electron Microscope (FESEM)

Surface morphological changes were examined after removing corrosion products from the mild steel specimens following ASTM G1-03 procedures [19] Corrosion product formation and changes in surface morphology were characterized using a field emission scanning electron microscope (FESEM; Brand: ZEISS, Model: Supra 55VP) operated at 15 kV with magnifications ranging from 170× to 1000×. Due to resource constraints, only selected samples were subjected to FESEM analysis. Sample selection was based on relevance to key temperature conditions and the availability of instrumentation. Specifically, samples exposed to the control temperature (25°C) in the absence of CO_2 and samples exposed to 80°C in both CO_2-saturated and non-saturated CO_2 NaCl environments were chosen for detailed observation. The 80°C condition was prioritized as it represents the highest testing temperature and closely approximates actual pipeline operating temperatures. Previous studies have reported that the average operating temperature of low-temperature pipeline segments in midstream sectors typically ranges between ~70°C and 230°C [11]

2.6. ImageJ software

The FESEM images were analysed using ImageJ software by adjusting the threshold to measure the porosity area and skeletonizing to measure the edge-length density (ELD) for texture proxy analysis. Crack length was quantified from skeletonized crack masks in which the segment length was taken as Feret length, the maximum calliper distance between two parallel lines tangent to the object outline. The total crack length equals the sum of segmented Feret lengths across the analysed field. Crystal size was expressed as the area-equivalent circular diameter of each detected object.

$$\text{ECD}=2\sqrt{\frac{A}{\pi}} \tag{2}$$

where A is the object's projected area in μm^2 and ECD is the standard diameter corresponding to a circle of equal projected area and is widely used for particle or crystal sizing from micrographs.[20] ECD distribution (h) was plotted with fixed bin edges shared by all conditions. The bin width followed the Freedman–Diaconis rule (skew and outliers) based on the ECD range in which corresponds to ~30 equal-width bins.[21]

$$h = \frac{2 \cdot IQR}{n^{1/3}} \tag{3}$$

Where IQR is the interquartile range and n is the number of crystallites.

2.7. Optical Microscope (OM)

Prior to cross-sectional analysis, the sample was coated with copper (Cu) via electroplating to preserve the corrosion scale during mounting [22] The Cu layer thus seen in cross-sections is a mounting aid, not a corrosion product. Then, it was embedded in a resin mould. The sample was then sectioned using a precision diamond cutter, and a cross-sectional image was captured using an optical microscope (Euromex Oxion Inverso Materials Science) at 50× magnification.

2.8. X-ray Diffraction (XRD)

Phase identification was performed using X-ray diffraction (XRD; Bruker, D8 Advance, Germany) operated within a 2θ range of 20°–70°. Table 2 presents a summary of the experimental conditions and analytical techniques employed in this study.

Table 2 Experimental parameters and analytical techniques for sweet corrosion study

Parameter	Test 1	Test 2
Environment	Presence of CO_2 gas	Absence of CO_2 gas
Electrolyte	3.5% NaCl solution	
Apparatus	1L glass cell	
Sample	Mild carbon steel grade SAE/AISI 1015	
Pressure (atm)	1 atm	
Temperature (°C)	40, 60, and 80	
Immersion/Exposure time (day)	7	
Surface analysis technique	FESEM, ImageJ, OM, and XRD	
Corrosion rate measurement	Weight loss method	

3. RESULTS AND DISCUSSIONS

3.1. Corrosion Rate

Table 3 summarizes the mass loss (mean ± SD) and the derived corrosion rates for each condition. For CO_2-saturated tests at 25–60°C, SD was 0.001–0.003 g (RSD ≈ 0.22–1.01%), indicating good repeatability of surface preparation, cleaning, and weighing. In the CO_2-free solution, the absolute losses are much smaller, thus the relative dispersion is higher (RSD ≈ 9.05–14.95%) despite similarly small absolute SD. At 80°C under a CO_2 environment, scatter increased (SD = 0.010 g; RSD = 6.28%), plausibly from heterogeneous $FeCO_3$ films formation and partial delamination.

Table 3 Average weight loss (g), standard deviation (SD), relative standard deviation (RSD), and corrosion rate (mm/y) for specimens tested at 25°C –80°C with and without CO_2 (n = 2)

Condition	Temperature (°C)	Mean weight loss (g)	SD (g)	RSD (%)	Corrosion rate (mm/y)
Presence of CO_2	25	0.1189	0.001	1.01	1.9736
	40	0.1792	0.003	1.50	2.9758
	60	0.2530	0.001	0.22	4.2013
	80	0.1520	0.010	6.28	2.5233
Absence of CO_2	25	0.0149	0.001	9.04	0.2466
	40	0.0350	0.005	14.95	0.5812
	60	0.0470	0.004	7.82	0.7805
	80	0.0677	0.007	9.81	1.1242

Figure 2 presents the corrosion rates of mild steel samples following a 7-day exposure to both CO_2-saturated and CO_2-free 3.5% NaCl solutions at 25°C (control), 40°C, 60°C, and 80°C. The corrosion rates of mild steel exposed to CO_2-saturated solution were significantly higher, ranging from 1.9736 mm/y to 4.2013 mm/y, compared to mild steel exposed to the CO_2-free environment, ranging from 0.2466 mm/y to 1.1242 mm/y. The dissolution reaction of steel occurs more significantly in the presence of CO_2, particularly within the transition and pre-passivation regions [23]

For the tests conducted in the absence of CO_2, the corrosion rate clearly increased with elevating temperature, with the highest corrosion rate observed at 80°C (1.1242 mm/y) compared to 25°C (0.2466 mm/y). Elevated temperatures enhanced the corrosion activity of steel by influencing the kinetics of the corrosion reactions [24] However, for the tests conducted in the presence of CO_2, mild steel exposed to 60°C showed the highest corrosion rate (4.2013 mm/year) compared to other temperatures. Studies reported that when the temperature was below 60°C, the formation of protective layers on the steel surface was hindered due to the high dissolution rate of the $FeCO_3$. At 80°C, the corrosion products likely precipitated densely onto the surface of the mild steel, forming a protective layer that subsequently reduced the corrosion rate from 4.2013 mm/y to 2.5233 mm/y. The corrosion rate decreased as a protective layer formed at temperatures above 60°C, where $FeCO_3$ precipitated, solidified, and adhered to the steel surface.[8]

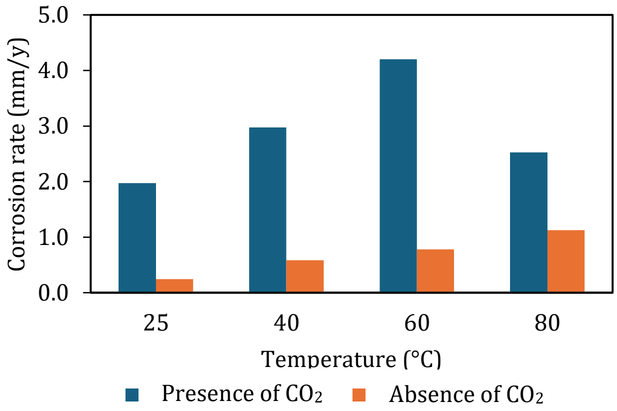

Figure 2. Corrosion rates of mild steel exposed to CO_2-saturated 3.5% NaCl solution and 3.5% NaCl solution without CO_2 at temperatures of 25°C, 40°C, 60°C and 80°C.

3.2. Surface Morphology

The FESEM images of the mild steel surface morphology after the removal of corrosion products according to ASTM G1-03 are presented in Figure 3. Under the control condition, CO_2-free at 25°C (Figure 3(a)), the morphology of the mild steel is predominantly uniform, relatively flat, and sparsely porous microstructure. Quantitative image analysis using ImageJ software on the 100 μm field (Figure 3 (b)) identified 81 discrete pores per field corresponding to a pore area fraction of 0.201%. Pore geometry is dominated by micro pits where the equivalent circular diameter (ECD) is 3.06 ± 1.08 μm and pores are nearly equiaxed (best-fit ellipse aspect ratio ≈ 1.33). The low pore area fraction, together with near unity aspect ratios, indicates isolated, shallow defects rather than elongated crevices or crack-like features. At 10 μm magnification, the edge-length density (ELD) calculated from the skeletonized FESEM image (Figure 3 (d)) is 0.8826 μm^{-1}, indicating a fine, discontinuous micro texture without a connected crack network.

The mild steel exhibited a significant morphological change from sparse, equiaxed micro pits to a high density of shallow, wide pits when exposed to 80°C without the presence of CO_2 (Figure 3(e-h)), where numerous pores were observed on the surface. ImageJ segmentation of the 100 µm field quantifies n = 1737 pores with an area porosity of 17.933 % indicating extensive localized attack over the field of view. The ECD broadens and shifts upward (mean 4.82 ± 7.84 μm) indicating pit growth and intermittent coalescence with a modest increase in elongation (best-fit ellipse aspect ratio ≈ 1.50). In a 10 μm field, the ELD derived from a skeletonized edge map increases markedly (1.1181 μm^{-1}) relative to the control, evidencing a busier but still discontinuous micro texture dominated by asperity and pit rims than a crack network.

At 80°C under a CO_2 environment (Figure 3(i-l)), the sample surface exhibited an uneven morphology with a rougher surface microstructure compared to the control sample. However, the formation of pores was not pronounced compared to the CO_2-free case. ImageJ segmentation of a 100 μm field detects n = 250 pores, giving the area porosity of 0.809%. Pores remain small and near equiaxed with ECD = 3.32 ± 1.66 μm and aspect ratio = 1.33. In contrast, the 10 μm field texture proxy (Figure 3(l)) is high yielding ELD = 2.253 $\mu m^{-1,}$ which is about twice the CO_2-free surface at 80°C and far above the control sample. The combination of suppressed open porosity and high ELD indicates a compact yet finely faceted surface film.

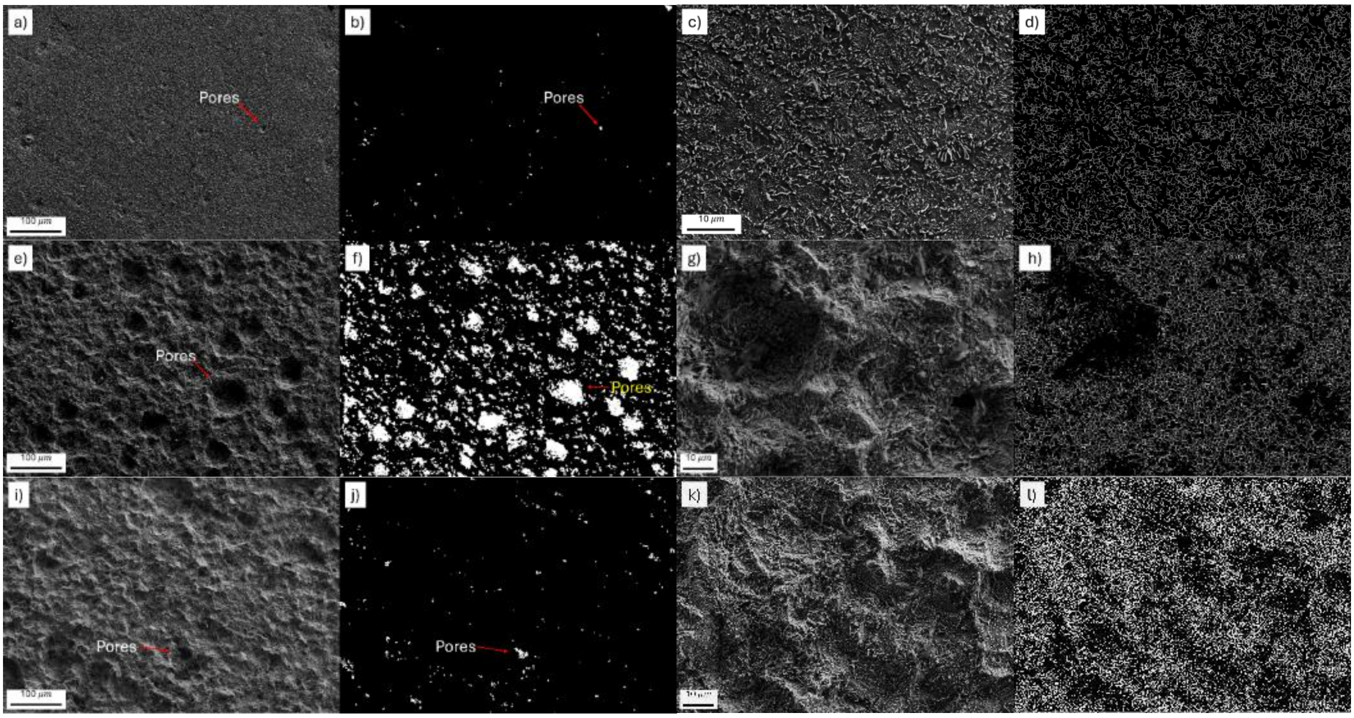

Figure 3. FESEM morphologies of the sample after corrosion product removal in 3.5 wt.% NaCl. (a–d) 25°C, CO_2-free (control): (a) 100 μm field, (b) pore mask, (c) 10 μm field, (d) skeletonized edge map; (e–h) 80°C, CO_2-free: (e) 100 μm field, (f) pore mask, (g) 10 μm field, (h) skeletonized edge map; (i–l) 80°C, CO_2-saturated: (i) 100 μm field, (j) pore mask, (k) 10 μm field and (l) skeletonized edge map.

The pH of the solution influences the characteristics and morphology in corrosion systems containing CO_2.[25] Figure 4 shows the pH readings for both the 3.5 wt.% NaCl solution saturated with CO_2 and without CO_2 over a 7-day immersion period at both control and 80°C temperatures. For the control sample, the pH readings remained stable on days 1 and 2, but there was a significant decrease on day 3, followed by an increase on day 4, and remained stable thereafter. The pH readings for the 3.5 wt.% NaCl solution without CO_2 at 80°C appeared more stable, ranging from 5.98 to 6.21, approaching the neutral range. Although the pH of the NaCl solution without CO_2 was higher compared to the CO_2-saturated environment, the corrosion observed on the surface of the mild steel appeared localized. Even under active corrosion conditions, a change in the pH from acidic to neutral or alkaline can induce a shift in the main cathodic reaction from hydrogen evolution to oxygen reduction. [26] Non-uniform corrosion commonly occurs under neutral or alkaline conditions due to the oxygen concentration cells formation with part of the steel being covered by corrosion products.

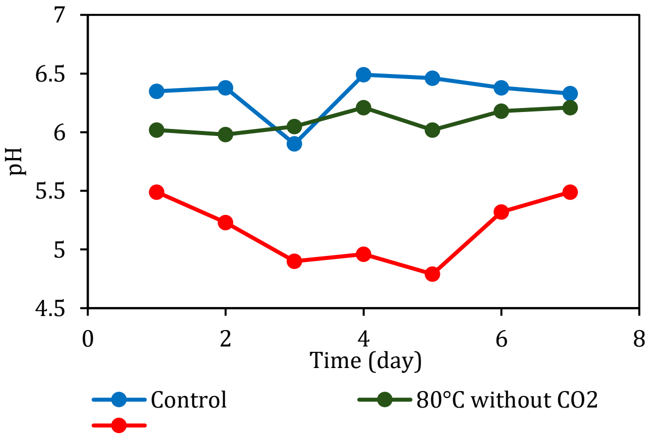

Figure 4. pH reading of the 3.5 wt.% NaCl solution over a 7-day immersion period.

The graph clearly indicates that the pH readings of the CO_2-rich brine solution at 80°C decreased significantly from day 1 to day 3, then increased on day 4, dropped once again on day 5, and then rose significantly on days 6 and 7. The pH range for the CO_2-saturated 3.5 wt.% NaCl solution was between 4.79 and 5.49. The initial pH drop during the early phase of the study was attributed to the dissolution of CO_2 in water, forming carbonic acid, which increased the acidity of the solution through the release of H^+ ions.[27] CO_2 corrosion of carbon steel is more severe in the initial stages compared to the later stages, resulting in a rapid pH decrease on the first day and a more stabilized pH thereafter.[9] Mild steel exposed to the CO_2-saturated 3.5 wt.% NaCl solution exhibited a higher corrosion rate compared to the environment without CO_2; however, the mild steel surface morphology did not display prominent pitting as seen in Figure 3 (e), despite being at the same temperature. This is because general corrosion on carbon steel often occurs in acidic solutions driven by the continuous interchange of anodic and cathodic sites.[26]

3.3. Microstructure of Corrosion Product

The microstructure of the corrosion products formed on the surface of mild steel was observed under a digital microscope and FESEM at 1,000× magnification, as shown in Figures 5 to 9. Figure 5 (a-b) presents the microstructure of the corrosion products formed on the control sample in the absence of CO_2. Based on Figure 5 (b), the corrosion products on the control sample exhibited a cigar-shaped crystal morphology. A small cluster of needle-like plate structures could also be observed among the cigar-shaped crystals. Based on FESEM analysis, the corrosion products likely formed on the steel surface were FeOOH. The microstructure of akaganeite (β-FeOOH) typically appears in the form of cigar-shaped crystals, rosettes, and whiskered rod structures, whereas goethite (α-FeOOH) commonly appears as needle-like structures and cotton ball-like morphologies .[28] ImageJ analysis identifies n = 2076 crystallites occupying 13.28% of the field. The crystal size distribution is right skewed with mean ECD = 0.786 ± 0.368 μm and IQR = 0.491-0.984 μm. Best-fit ellipse shapes (median aspect ratio = 1.42) show mild elongation without a preferred orientation. These values and morphologies are consistent with FeOOH polymorphs (akaganeite $\approx 2.2 \pm 0.15$ μm; goethite ≈ 0.5-1 μm) found on steels in chloride media .[29], [30]

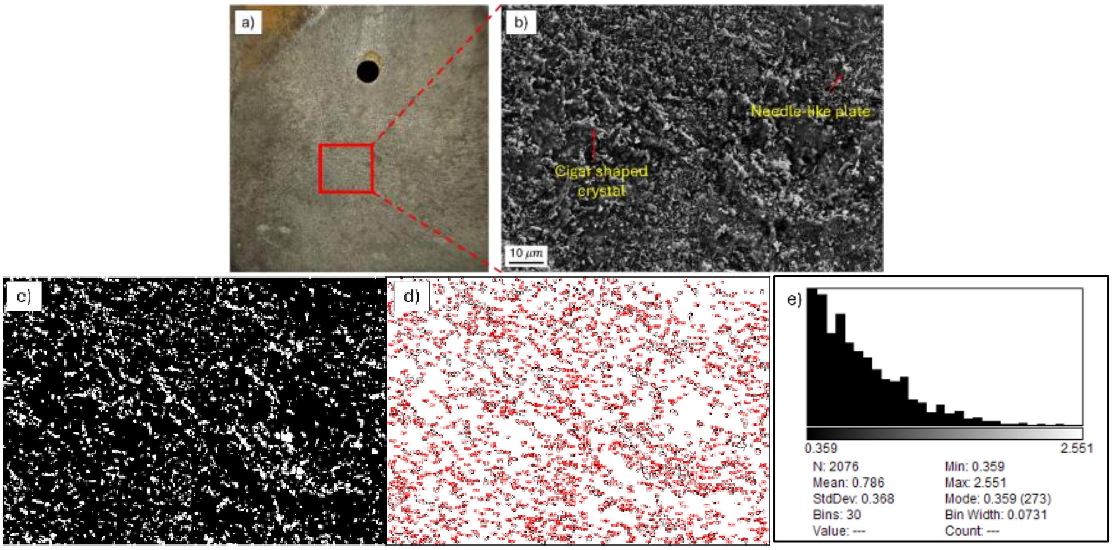

Figure 5. Corrosion products morphology at 25°C under CO_2-free environment (a) Macroscopic image (b) FESEM image at 1,000 magnification (c) binary crystallite mask (d) schematic outline of detected crystallites (e) ECD histogram.

Figures 6 and 7, respectively, present the FESEM images of the corrosion products formed on the surface of mild steel at 80°C without the presence of CO_2, captured at two distinct locations designated as points A and B. Both locations clearly reveal the presence of cracks on the mild steel surface. The formation of pits due to localized corrosion acts as initiation sites for crack development, with the cracks subsequently propagating into the surrounding areas .[31] Corrosion product deposition was observed within the cracks, potentially serving as active sites for further localized corrosion. The corrosion products at point A (Figure 6 (b)) and point B (Figure 7 (b)) exhibited similar microstructures, characterized by fibrous and cotton ball-like morphologies. However, the amount of corrosion products formed at point A was noticeably greater compared to that at point B.

At point A (Figure 6(b-e)), the corrosion scale is traversed by a dense, cross-linked crack network. Skeleton analysis (Figure 6(d)) gives a total crack path length of 233.176 μm within the analysed field (area crack length density = 0.02521 μm^{-1}). Several cracks are partially filled by corrosion product, consistent with shrinkage and mismatch stress cracking of compact layers composed of FeOOH and magnetite in hot aqueous media .[32] ImageJ particle analysis (Figure 6(f-g)) resolves a fine sub-micron to low micron crystallite population (n = 2409) with a mean ECD of 0.844 ± 0.441 μm covering 18.54% of the field. The ECD distribution (Figure 6(h)) is right-skewed with median = 0.728 μm and IQR = 0.507-1.061 μm. Best-fit ellipse shape metrics show elongated crystallites (median aspect ratio is 1.582), which is consistent with the clustered cotton-ball aggregates associated with goethite in aerated, CO_2-free environments on carbon steel .[33]

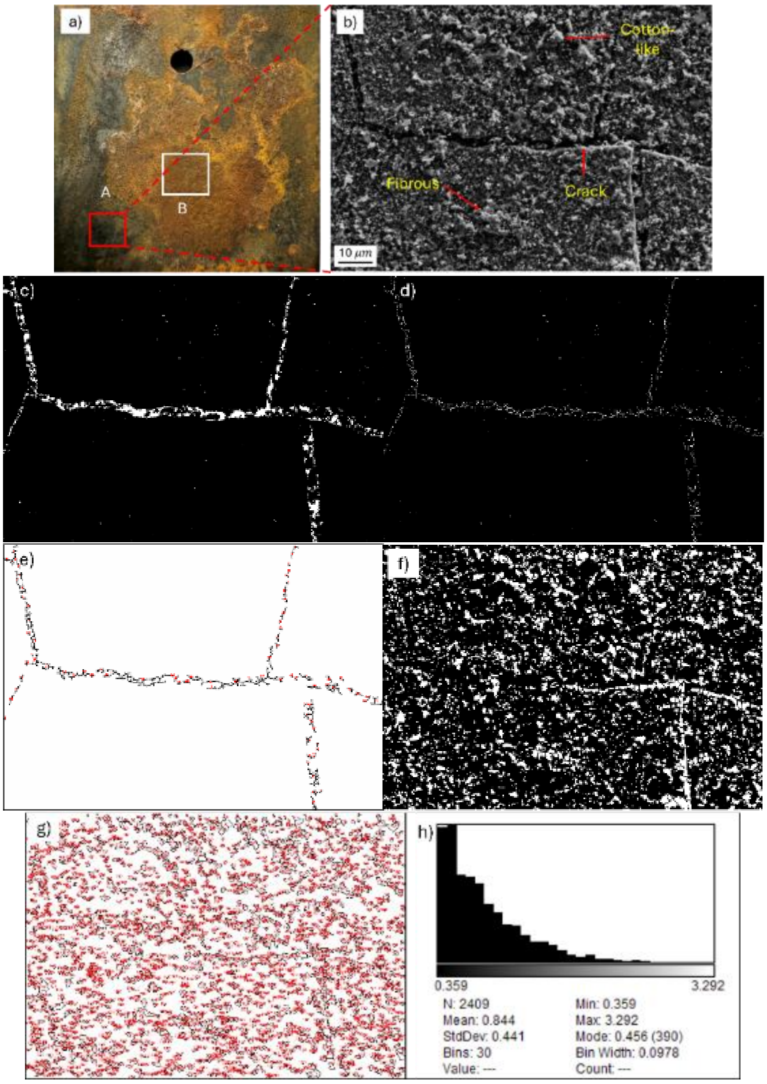

Figure 6. Corrosion products morphology at 80°C under CO_2-free environment at point A (a) Macroscopic image (b) FESEM image at 1,000 magnification (c) binary crack mask (d) skeletonized crack map (e) schematic outline of detected crack (f) binary crystallite mask (g) schematic outline of detected crystallites (h) ECD histogram.

While at point B (Figure 7(b-e)), the total crack length is 222.924 μm, giving an area crack length density = 0.02410 μm^{-1} within the analysed field. Analysis of watershed-segmented crystallites at point B (Figure 7(f-g)) identifies n = 1447 particles with a mean ECD = 0.974 ± 0.363 μm, median = 0.887 μm, and IQR = 0.671-1.209 μm. The crystallites occupy 13.30% of the field. The ECD distribution is right-skewed, indicating a dominant fine fraction with a short coarse tail. Best-fit ellipse shape metrics show elongated particles with a median aspect ratio = 1.538. Compared to point A, point B shows a less dense crack network (point A = 0.02521 μm^{-1}; point B = 0.02410 μm^{-1}) and a coarser (median point A = 0.728 μm; median point B = 0.887 μm) but sparser crystallite population (point A = 18.54%; point B = 13.30%) while preserving the same FeOOH type morphology.

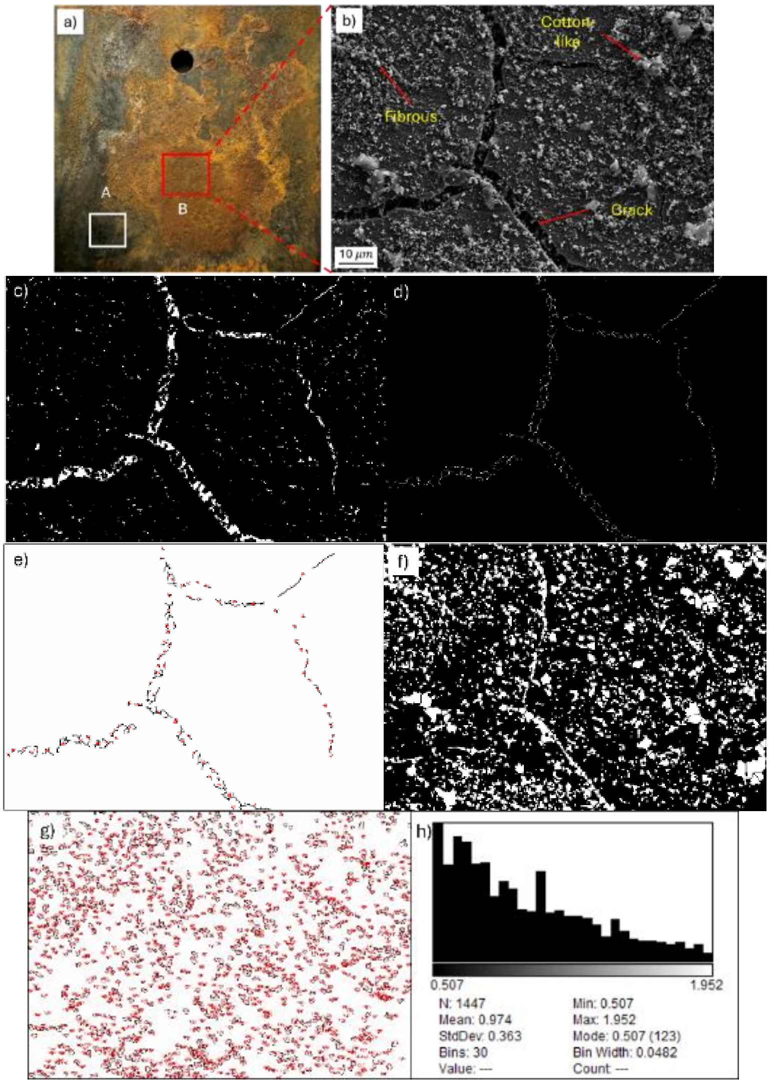

Figure 7. Corrosion products morphology at 80°C under CO_2-free environment at point B (a) Macroscopic image (b) FESEM image at 1,000 magnification (c) binary crack mask (d) skeletonized crack map (e) schematic outline of detected crack (f) binary crystallite mask (g) schematic outline of detected crystallites (h) ECD histogram,

The microstructure of corrosion products formed on mild steel exposed to a CO_2-saturated environment at 80°C was observed at two distinct points, A (Figure 8) and B (Figure 9), as visual analysis revealed significant differences in colour and surface structure. Based on Figure 8 (b-d), the corrosion products formed at point A in 3.5 wt.% NaCl saturated with CO_2 exhibits a prismatic morphology with trigonal-pyramidal apexes. According to Kindi, [13] siderite ($FeCO_3$) typically exhibits a microstructure characterised by microfaceted cylindrical crystals with trigonal-pyramidal caps. ImageJ analysis identifies n = 325 crystallites covering 57.4% of the field. The ECD is strongly right-skewed with mean = 3.309 ± 3.065 μm, median = 2.109 μm, and IQR = 1.189-4.259 μm, aligned with past studies where the crystal size of $FeCO_3$ is typically in the range of ∼2.0-22.0 μm .[34]–[36] Best-fit ellipse metrics indicate moderate elongation (median aspect ratio = 1.566), consistent with the prismatic habit observed in Figure 8 (b).

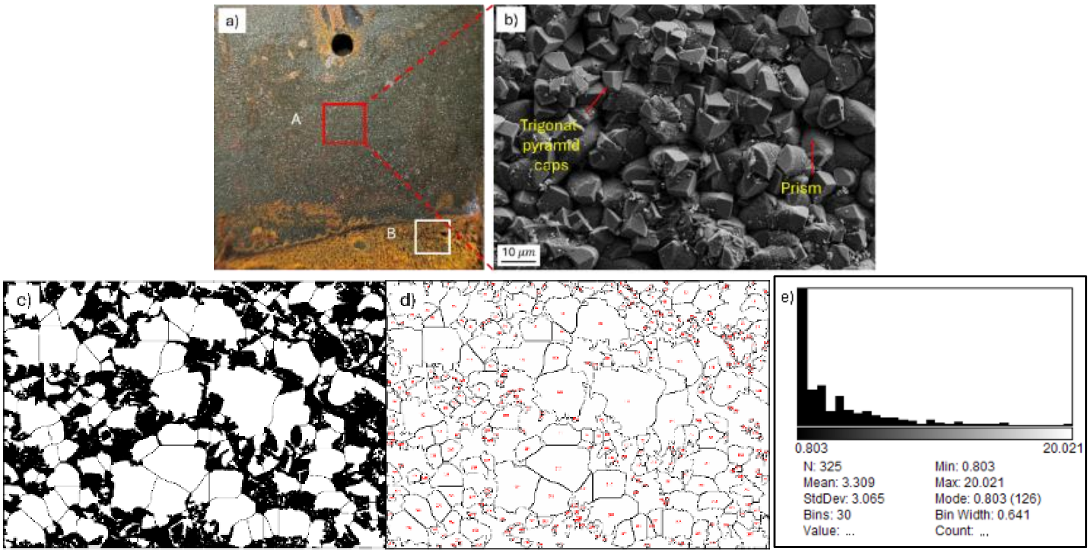

Figure 8. Corrosion products morphology at 80°C under CO_2-saturated environment at point A (a) Macroscopic image (b) FESEM image at 1,000 magnification (c) binary crystallite mask (d) schematic outline of detected crystallites (e) ECD histogram.

In contrast, the corrosion products observed at point B (Figure 9 (b)) display a distinctly different morphology where the products predominantly exhibit a needle-like structure. The corrosion product formed at point B is likely chukanovite ($Fe_2(OH)_2CO_3$) as it is reported to exhibit fibrous, needle-like, or plate-like structures.[34] Furthermore, Dhaiveegan et al. [28] reported that goethite (α-FeOOH) can also manifest in a needle-like morphology.

Particle analysis detects n = 1680 crystallites occupying 28.15% of the field. The mean ECD is 1.198 ± 0.703 μm, median = 1.01 μm, and IQR = 0.58-1.53 μm, yielding a clearly right-skewed distribution. Best-fit ellipse analysis shows systematic elongation with a median aspect ratio = 1.48. This finding aligns with other studies where the crystal size of goethite is in the range of 1-5 μm [37] and the chukanovite crystal size of ~2 μm .[34]

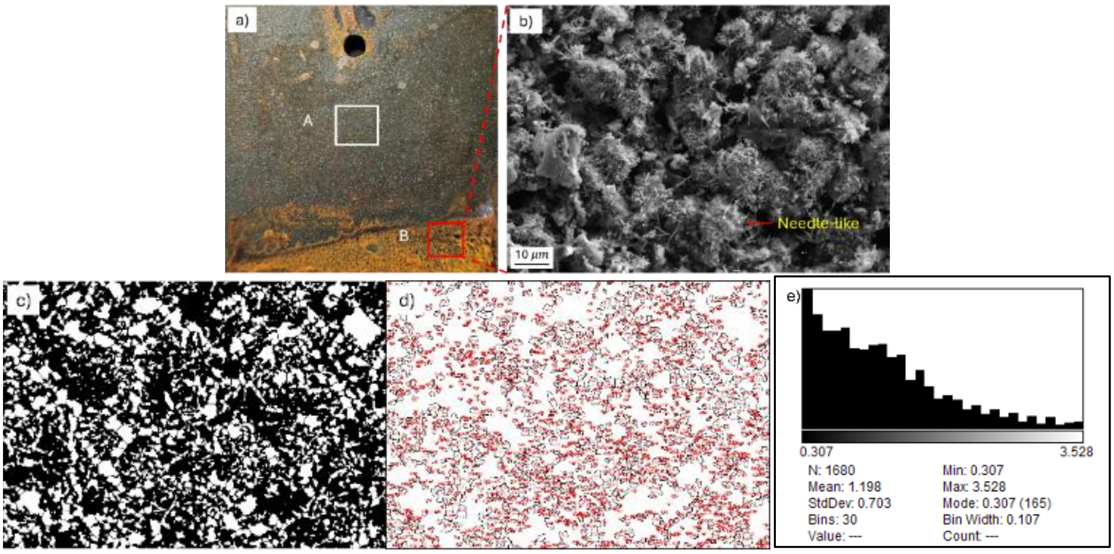

Figure 9. Corrosion products morphology at 80°C under CO_2-saturated environment at point B (a) Macroscopic image (b) FESEM image at 1,000 magnification (c) binary crystallite mask (d) schematic outline of detected crystallites (e) ECD histogram.

3.4. Cross-sectional Analysis

Cross-sectional analysis was performed using optical microscopy (OM) to investigate the effect of temperature and CO_2 exposure on the thickness of the corrosion product layer. Figures 10 and 11 show the cross-sectional images of samples exposed to two different media: without CO_2 and with CO_2 at various temperatures (25°C, 40°C, 60°C, and 80°C). Temperature significantly affects the crystal size and thickness of corrosion product layers .[8] As shown in Figure 10, the corrosion product thickness increases with increasing temperature. A thin corrosion product layer can be clearly observed at 25°C (22 μm) (Figure 10 (a)) and at 40°C (33 μm) (Figure 10 (b)). At both 25°C and 40°C, the formed corrosion product layers appear porous and loosely packed. This indicates the corrosion products are ineffective in preventing further corrosion of the mild steel surface. Shi et al. (2018) reported that lepidocrocite (γ-FeOOH) and hematite (α-Fe_2O_3), which possess porous structures, are unstable and do not provide effective protection to the steel surface.

At higher temperatures, specifically at 60°C (Figure 10 (c)) and 80°C (Figure 10 (d)), the corrosion product layer appeared denser, more robust, and thicker. However, the presence of pores and cracks was still observed, which could serve as pathways for corrosive species to penetrate the mild steel surface and thus promote further corrosion. Previous studies reported that the oxygen concentration at the bottom of the pores is significantly low and gradually increases along the outward path, whereas the concentration of chloride ions (Cl^-) is very high at the pore bottom and progressively decreases towards the surface .[39] Ferrous ions (Fe^{2+}) can also diffuse outward through these pores and react with free hydroxide ions (OH^-) present in the solution. The accumulation of corrosive species within these pores facilitates localized attack on the mild steel surface, ultimately leading to the initiation and propagation of localized corrosion.

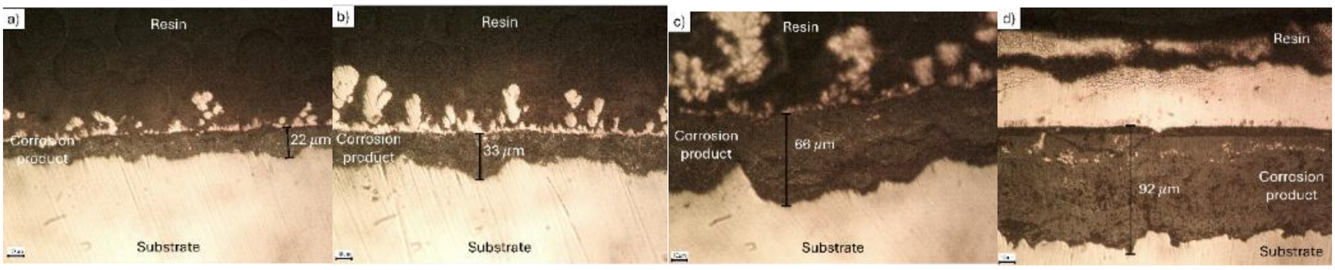

Figure 10. Cross-sectional images of mild steel exposed to 3.5 wt.% NaCl solution without the presence of CO_2 at temperatures of (a) 25°C, (b) 40°C, (c) 60°C and (d) 80°C.

In the CO_2 environment, the thickness of the corrosion product layer increased significantly from the control temperature to 60°C; however, the layer thickness at 80°C was lower compared to that at 60°C. As shown in Figures 11 (a) and (b), the corrosion product layer exhibited a denser structure at the bottom region but appeared porous in the upper region. This phenomenon can be attributed to the formation of porous and amorphous corrosion products at lower temperatures, which provide poor protection to the steel surface .[40] The upper layer, being directly exposed to the corrosive solution, is more prone to dissolve into the electrolyte, resulting in the formation of a thinner corrosion product layer.

The thickest corrosion product layer in the CO_2 environment was formed at 60°C (Figure 11 (c)). This observation is consistent with the high corrosion rate experienced by mild steel under these conditions. At this temperature, the corrosion products began to solidify densely and uniformly across the steel surface. At 80°C, the thickness of the corrosion product layer was lower but exhibited greater compactness. The surface of the mild steel was covered with cylindrical-shaped corrosion products featuring trigonal-pyramidal apexes at the upper layer, while a more homogeneous layer was formed at the lower region. The reduced corrosion rate and lower layer thickness indicate that the corrosion products acted as a protective barrier for the mild steel. Previous studies have reported that at temperatures exceeding 70°C and pH levels around 6, corrosion products rapidly form protective layers, leading to a decrease in corrosion rate .[41]

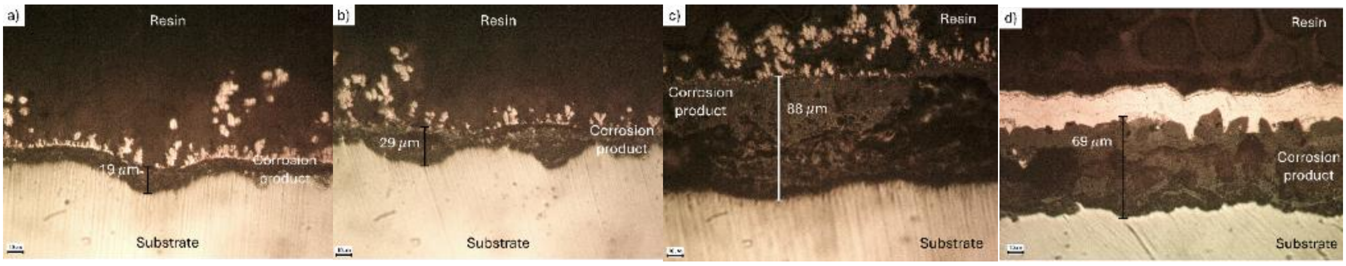

Figure 11. Cross-sectional images of mild steel exposed to 3.5 wt.% NaCl solution with the presence of CO_2 at temperatures of (a) 25°C, (b) 40°C, (c) 60°C and (d) 80°C.

3.5. XRD Analysis

XRD analysis was conducted to obtain detailed information on the chemical composition and crystallographic structure of the formed corrosion products. Changes in the intensity of Fe peaks between the original and tested samples indicate that reactions occurred between the mild steel and the surrounding environment. For the environment without CO_2 (Figure 12), the corrosion product phases detected at the control temperature were NaCl and hematite (Fe_2O_3), appearing at 2θ = 31.742° on the (200) plane (PDF01-079-9877) and at 2θ = 35.522° on the (110) plane (PDF00-056-1302), respectively. The presence of the NaCl phase is attributed to the evaporation of the 3.5 wt.% NaCl solution, resulting in NaCl crystals adhering to the surface of the mild steel. The formation of Fe_2O_3 is attributed to the oxidation of $Fe(OH)_2$.[42]

At a temperature of 80°C, the most prevalent phase formed is cementite (Fe_3C) with a major peak occurring at 2θ = ~37°-60° (JCPDS, 76-1877; PDF01-076-1877). This indicates that the corrosion rate of the sample at 80°C in the

CO_2-free environment is higher compared to other temperatures, as Fe_3C has a brittle, porous, and non-adherent structure that can easily be removed by flow .[9] This phase is also predominantly detected because Fe_3C is an existing compound in the composition of mild steel. The corrosion process causes the dissolution of the ferrite phase, exposing the Fe_3C network to the environment .[43] Other phases detected on the surface of mild steel include FeOOH at 2θ = 30.206° (220) and 62.813° (440) (PDF01-074-3080), Fe_2O_3 at 2θ = 27.941° (002), 35.522° (110) and 56.548° (113) (PDF00-056-1302) 27.941° and NaCl at 2θ = 31.742° (200) and 45.505° (220) (PDF01-079-9877).

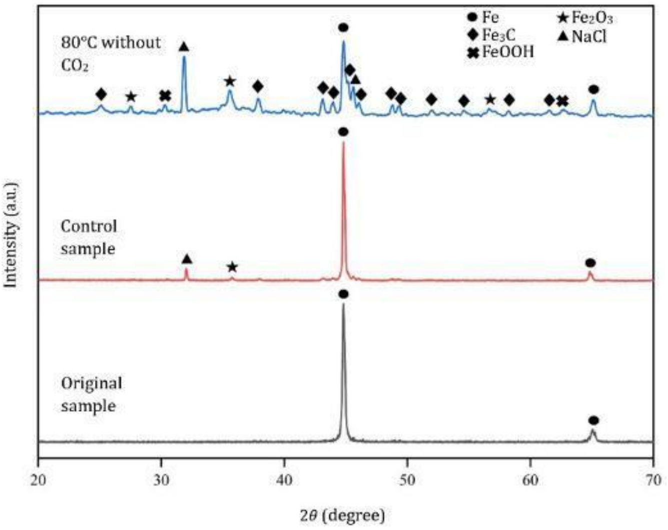

Figure 12. XRD diffractogram of mild steel in 3.5 wt.% NaCl solution without the presence of CO_2.

Ferric hydroxide can oxidize to form FeOOH, Fe_2O_3, and Fe_3O_4 compounds. FeOOH is a hydrated form of Fe_2O_3 and has subtypes such as goethite (α-FeOOH), akaganeite (β-FeOOH), and lepidocrocite (γ-FeOOH) .[42] The reactions occurring on the surface of mild steel in the CO_2-free environment are illustrated in equations below.

$$2H_2O + 2e^- \rightarrow H_2\,(g) + 2OH^- \tag{4}$$

$$Fe\,(s) + 2OH^- \rightarrow Fe(OH)_2\,(s) + 2e^- \tag{5}$$

$$4Fe(OH)_2 + O_2 + 2H_2O \rightarrow 4Fe(OH)_3 \tag{6}$$

$$2Fe(OH)_3 \rightarrow Fe_2O_3 + H_2O \tag{7}$$

$$Fe_2O_3 + 2H_2O \rightarrow 2FeOOH \tag{8}$$

Figure 13 shows the XRD diffractogram of mild steel in a CO_2 environment at control temperature and 80°C. Based on the spectrum of the control sample, it clearly shows the presence of Fe_3C on the surface of the control sample, with the major peak occurring at 2θ = ~37°-58° (PDF01-076-1877). According to Zulkafli et al. [9], Fe_3C is a corrosion product frequently found in the reaction between mild steel and a CO_2 environment. The formation of the Fe_3C network on the steel surface during the sweet corrosion process occurs during the initial stages of CO_2 dissolution in the solution, after which it will be covered by a layer of $FeCO_3$.[44] The formation of the $Fe(OH)_2$ phase can be detected at 2θ = 31.767° (100), 52.144° (012), and 56.593° (110) (PDF01-073-6991). $Fe(OH)_2$ forms through the following reaction:

$$Fe\,(s) + 2H_2O \rightarrow Fe(OH)_2\,(s) + 2H^+\,(aq) + 2e^- \tag{9}$$

According to Fonseca et al. [45], the presence of the porous $Fe(OH)_2$ layer prior to the formation of $FeCO_3$ occurs in low O_2 electrolytes at pH 4. $Fe(OH)_2$ acts as a precursor for the formation of $FeCO_3$, where the porous structure of $Fe(OH)_2$ allows the siderite layer to grow outside the existing hydroxide corrosion scale. Equations (10) and (11) show the reactions for the formation of $FeCO_3$ from the existing $Fe(OH)_2$.

$$Fe(OH)_2\,(s) + CO_2 \rightarrow FeCO_3\,(s) + H_2\,(g) \tag{10}$$

$$Fe(OH)_2\,(s) + H_2CO_3\,(aq) \rightarrow FeCO_3\,(s) + H_2O\,(l) \tag{11}$$

At an ambient temperature of 80°C, the formation of the siderite phase, also known as $FeCO_3$, is observed at 2θ = 24.763° (012), 32.023° (104), and 38.340° (110), which is highly consistent with the PDF01-083-1764 database. $FeCO_3$ is a corrosion product that can provide a protective layer to steel at high temperatures. Therefore, this suggests that the reduction in corrosion rate and the thickness of the corrosion products in this environment is due to the formation of the $FeCO_3$ layer on the steel surface. Corrosion studies of carbon steel in a CO_2-saturated NaCl environment found that Fe_3O_4 and $FeCO_3$ are the dominant compounds in the corrosion products .[8] The hematite phase (Fe_2O_3) is also detectable on the steel surface at 2θ = 35.739° (321) (PDF01-074-6271). The formation of Fe_2O_3 occurs due to the presence of O_2 in the environment, causing the dense $FeCO_3$ layer to react with O_2 to form a porous Fe_2O_3 corrosion product .[44] The formation of Fe_2O_3 occurs when mild steel is removed from a CO_2-saturated NaCl solution, exposing the steel to an environment containing O_2 gas. The reaction between $FeCO_3$ and O_2 is given in the equation below:

$$4FeCO_3 + O_2 \rightarrow 2Fe_2O_3 + 4CO^{2-} \quad (12)$$

In addition, the formation of NaCl compounds can be observed at 2θ = 31.762° (200) due to the high temperature, which causes the evaporation of the 3.5% NaCl solution, leading to the formation of NaCl crystals on the mild steel surface (PDF01-071-4661).

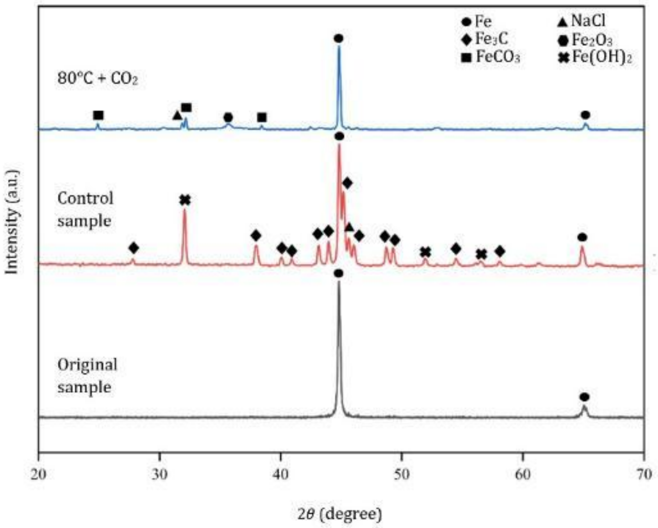

Figure 13. XRD diffractogram of mild steel in CO_2-saturated 3.5 wt.% NaCl solution.

3.6. Arrhenius Model

Arrhenius model (Figure 14-15) was employed to derive theoretical predictions for corrosion rates across a temperatures in both electrolytes. The corrosion rate (CR) is exponentially related to the temperature. Higher temperatures provide more energy for the atoms or molecules involved in the corrosion process, making the reaction occur more rapidly. The relationship between the corrosion rate and temperature is described by the Arrhenius equation [46]:

$$\text{Ln(CR)=Ln(A)-}\frac{E_a}{RT} \quad (13)$$

where Ln(CR) is the natural logarithm of corrosion rate, A is the pre-exponential factor, E_a is the activation energy, R is the universal gas constant (8.3145 $Jmol^{-1}K^{-1}$), and T is the temperature in Kelvin.

In the CO_2-free environment (Figure 14), the model exhibited a good fit with an R^2 value of 0.922. This indicates the temperature-driven corrosion mechanism is well described by the Arrhenius equation, making it a suitable model for understanding the corrosion behaviour of mild steel in CO_2-free 3.5 wt.% NaCl solution. The experimental plot for the corrosion rate aligns with the theoretical prediction. Higher temperatures enhance atomic mobility, facilitating the dissolution of the steel and leading to accelerated corrosion.

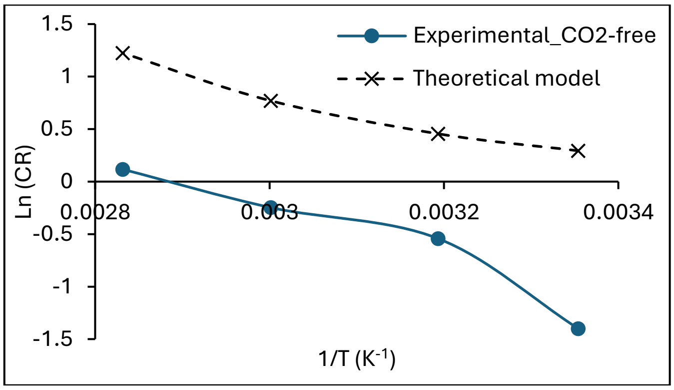

Figure 14. Arrhenius Model for corrosion rate in CO_2-free environment.

However, for the CO_2-saturated conditions (Figure 15), a modified Arrhenius model was employed to account for the effect of a protective $FeCO_3$ film that forms at elevated temperatures, thereby reducing the corrosion rate. The modified model is expressed as [46]:

$$\text{Ln(CR)=Ln(A)-}\frac{E_a}{RT}\cdot\text{f(T)} \quad (14)$$

$$f(T) = \{1, \quad T \leq 333.15K\ 0.72, \quad T > 333.15K \quad (15)$$

where f(t) is the reduction factor for protective film. The model shows an R^2 value of 0.4778, indicating a relatively poor fit to the experimental data. While the model accounts for this effect using a reduction factor, [47] it fails to fully capture the complexities of scale formation and its impact on corrosion. Previous studies have shown that $FeCO_3$ films formed at elevated temperatures can provide partial protection, but their protective efficiency is strongly dependent on factors such as supersaturation, pH stability, and flow regime.[48], [49] Hence, the single-step reduction factor is insufficient to capture the dynamic and heterogeneous nature of $FeCO_3$ film formation. More advanced semi-empirical models that incorporate precipitation kinetics, film porosity, and transport effects may be required to better describe corrosion behavior under CO_2-saturated conditions.

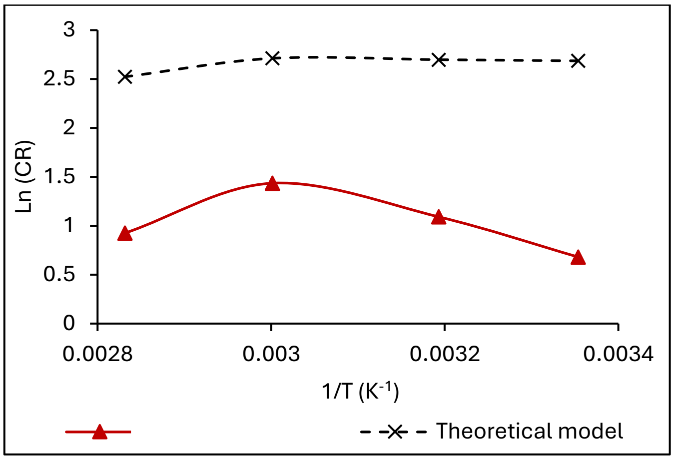

Figure 15. Arrhenius Model for corrosion rate in CO_2-saturated environment.

This study emphasises temperature influence on CO_2 corrosion, particularly the formation of protective $FeCO_3$ layers. The findings can be applied to nanomaterials research, especially in the development of advanced coatings or protective layers. Understanding the mechanism behind the formation of $FeCO_3$ at elevated temperatures provides valuable insight into designing nano-based corrosion inhibitors or coatings that mimic the protective properties of $FeCO_3$, offering a more efficient and sustainable solution to CO_2 corrosion.

4. CONCLUSION

The CO_2 corrosion behaviour of mild steel is influenced by environmental temperature. It was observed that corrosion under CO_2 conditions increases with temperature, reaching its highest rate at 60°C, but then slows down at higher temperatures due to the development of a protective $FeCO_3$ layer. Even at the same temperature, the presence of CO_2 consistently produced a higher corrosion rate than that observed in the absence of CO_2. Surface morphology observations revealed that mild steel subjected to a CO_2 environment at elevated temperatures experienced uniform corrosion with increased surface roughness, whereas mild steel exposed to a CO_2-free environment exhibited localized corrosion. This phenomenon is attributed to the influence of pH, where the carbonic acid formation reduces the pH, thereby promoting uniform corrosion. Cross-sectional analysis indicated that the thickness of the corrosion product layer increased with elevated temperature. However, at higher temperatures in the presence of CO_2, the thickness was moderate. XRD analysis identified the formation of siderite, cementite, hematite, and iron hydroxide phases in the CO_2 environment, whereas the corrosion products formed in the absence of CO_2 were cementite, hematite, and iron oxide hydroxide. Overall, elevated temperatures accelerate sweet corrosion processes unless corrosion products form a protective barrier, which has significant implications for industries operating under such environmental conditions.

ACKNOWLEDGMENTS

The authors acknowledge the financial support by Universiti Kebangsaan Malaysia (ST-2024-037) and Universiti Malaysia Terengganu (UMT/MGI+2/2024/UMT-UKM-RSU-Development and Testing of Corrosion Inhibitor for Marine Metal-vot 53594). Sincere appreciation is also extended to DNV GL@UKM for access to laboratory facilities.

REFERENCES

[1] E. J. da Cruz Junior et al., “Impact of Heat Input on the Cladding of Super Austenitic Stainless Steel Through the Gas Tungsten Arc Welding Process on ASTM A516 Grade 70 Steel,” Coatings, vol. 14, no. 11, 2024.

[2] M. F. Mamat et al., “Preparation of Linseed Oil-Filled Urea–Formaldehyde Microcapsules and Anti-Corrosion Performance of Self-Healing Epoxy Coatings on Low Carbon Steel Substrate,” Int. J. Nanoelectron. Mater., vol. 17, no. Special issue, pp. 61–70, 2024.

[3] S. M. Z. Hossain et al., “Cinnamaldehyde as a Green Inhibitor in Mitigating AISI 1015 Carbon Steel Corrosion in HCl,” Arab. J. Sci. Eng., vol. 44, no. 6, pp. 5489–5499, 2019.

[4] G. Ma et al., “The Effects of Microalloying on the Precipitation Behavior and Strength Mechanisms of X80 High-Strength Pipeline Steel under Different Processes,” Crystals, vol. 13, no. 5, 2023.

[5] J. Tang, R. Guo, X. Zhang, and X. Zhao, “Effect of Pseudomonas aeruginosa on corrosion of X65 pipeline steel,” Heliyon, vol. 8, no. 12, p. e12588, 2022.

[6] A. H. Alamri, “Localized corrosion and mitigation approach of steel materials used in oil and gas pipelines – An overview,” Eng. Fail. Anal., vol. 116, no. June, p. 104735, 2020.

[7] V. Sridharan, “Measurement of carbon dioxide corrosion on carbon steel using electrochemical frequency modulation,” 2009.

[8] S. Li, Z. Zeng, M. A. Harris, L. J. Sánchez, and H. Cong, “CO2 corrosion of low carbon steel under the joint effects of time-temperature-salt concentration,” Front. Mater., vol. 6, no. February, pp. 1–17, 2019.

[9] R. Zulkafli, N. K. Othman, and N. Yaakob, “Pencirian Permukaan Kakisan Keluli Karbon dengan Kehadiran Konsortium Bakteria Penurun Sulfat dalam Persekitaran Bergas CO2,” Sains Malaysiana, vol. 51, no. 9, pp. 3113–3123, 2022.

[10] R. Elgaddafi, R. Ahmed, and S. Shah, “Corrosion of carbon steel in CO2 saturated brine at elevated temperatures,” J. Pet. Sci. Eng., vol. 196, p. 107638, Jan. 2021.

[11] Y. T. Al-Janabi, “An overview of corrosion in oil and gas industry: Upstream, midstream and downstream sectors,” Corros. Inhib. Oil Gas Ind., pp. 3–39, 2020.

[12] M. A. Sadeghi and M. Javidi, “Investigation on stress corrosion cracking of API 5L X65 steel in CO2 corrosion medium,” Mater. Sci. Eng. A, vol. 824, no. August, p. 141856, 2021.

[13] M. Al Kindi, “Oilfield Corrosion: Sweet Corrosion Scales,” The University of Manchester, 2020.

[14] ASTM International, “Standard for the Preparation of Substitute Ocean Water,” D 1141, vol. 98, no. Reapproved, pp. 98–100, 2003.

[15] M. Singer, “Study of the localized nature of top of the line corrosion in sweet environment,” Corrosion, vol. 73, no. 8, pp. 1030–1055, 2017.

[16] S. Richter, M. Achour, K. Addis, M. Singer, S. Nesic, and M. Technology, “Development and Application of a Downhole Corrosion Prediction Model,” in NACE - International Corrosion Conference Series, 2016, no. 7827, pp. 1–15.

[17] S. K. Kairy, S. Zhou, A. Turnbull, and G. Hinds, “Corrosion of pipeline steel in dense phase CO2 containing impurities: A critical review of test methodologies,” Corros. Sci., vol. 214, p. 110986, Apr. 2023.

[18] ASTM International, “G31-72: Standard Practice for Laboratory Immersion Corrosion Testing of Metals,” An Am. Natl. Stand., vol. 03.02, pp. 1–8, 2012.

[19] ASTM International, “ASTM G1-03 Standard Practice for Preparing, Cleaning, and Evaluating Corrosion Test Specimens,” An Am. Natl. Stand., vol. 03.02, pp. 1–9, 2017.

[20] ASTM International, “Standard terminology relating to nonsieving methods of powder characterization,” no. March, pp. 22–23, 2023.

[21] D. Freedman and P. Diaconis, “On the histogram as a density estimator: L2 theory,” Zeitschrift für Wahrscheinlichkeitstheorie und Verwandte Gebiete, vol. 57, no. 4, pp. 453–476, 1981.

[22] ASTM International, “ASTM E3 Standard Practice for Preparation of Metallographic Specimens.” p. 8, 2017.

[23] A. Kahyarian and S. Nesic, “A New Narrative for CO2 Corrosion of Mild Steel,” J. Electrochem. Soc., vol. 166, no. 11, pp. C3048–C3063, 2019.

[24] Y. Liu, Z. Gao, X. Lu, and L. Wang, “Effect of Temperature on Corrosion and Cathodic Protection of X65 Pipeline Steel in 3.5% NaCl Solution,” Int. J. Electrochem. Sci., vol. 14, no. 1, pp. 150–160, 2019.

[25] F. Pessu, R. Barker, and A. Neville, “The influence of pH on localized corrosion behavior of X65 carbon steel in CO2-saturated brines,” Corrosion, vol. 71, no. 12, pp. 1452–1466, 2015.

[26] Y. Xu, Q. Zhang, H. Chen, Y. Zhao, and Y. Huang, “Experimental study on erosion-corrosion of carbon steel in flowing NaCl solution of different pH,” J. Mater. Res. Technol., vol. 20, pp. 4432–4451, 2022.

[27] R. Barker et al., “Iron carbonate formation kinetics onto corroding and pre-filmed carbon steel surfaces in carbon dioxide corrosion environments,” Appl. Surf. Sci., vol. 469, pp. 135–145, Mar. 2019.

[28] P. Dhaiveegan, N. Elangovan, T. Nishimura, and N. Rajendran, “Weathering Steel in Industrial-Marine-Urban Environment: Field Study,” Mater. Trans., vol. 57, no. 2, pp. 148–155, 2016.

[29] H. Khalid, S. G. Heo, W. S. Yang, B. S. Kim, T. S. Kim, and S. J. Seo, “Synthesis of 1-D iron oxide nano-sticks: Tuning the interfacial defects and surface of nano-sticks for fine-tuned exchange biasing,” J. Alloys Compd., vol. 801, pp. 199–207, 2019.

[30] L. Notini, L. K. Thomasarrigo, R. Kaegi, and R. Kretzschmar, “Coexisting Goethite Promotes Fe(II)-Catalyzed Transformation of Ferrihydrite to Goethite,” Environ. Sci. Technol., vol. 56, no. 17, pp. 12723–12733, 2022.

[31] J. A. Balbín, V. Chaves, and N. O. Larrosa, “Pit to crack transition and corrosion fatigue lifetime reduction estimations by means of a short crack microstructural model,” Corros. Sci., vol. 180, no. December 2020, p. 109171, 2021.

[32] R. Chawuthai et al., “Novel method for predicting the cracks of oxide scales during high temperature oxidation of metals and alloys by using machine learning,” Sci. Rep., vol. 15, no. 1, pp. 1–15, 2025.

[33] J. Alcántara, D. de la Fuente, B. Chico, J. Simancas, I. Díaz, and M. Morcillo, “Marine atmospheric corrosion of carbon steel: A review,” Materials (Basel)., vol. 10, no. 4, 2017.

[34] T. Koo and J. Kim, “Controls on the Formation and Stability of Siderite (FeCO3) and Chukanovite (Fe2(CO3)(OH)2) in Reducing Environment,” vol. 2, 2020.

[35] R. Neerup, I. A. Løge, and P. L. Fosbøl, "FeCO3 Synthesis Pathways: The Influence of Temperature, Duration, and Pressure," ACS Omega, vol. 8, no. 3, pp. 3404–3414, 2023.

[36] J. Owen, F. Ropital, G. R. Joshi, J. Kittel, and R. Barker, "Galvanic effects induced by siderite and cementite surface layers on carbon steel in aqueous CO2 environments," Corros. Sci., vol. 209, no. June, p. 110762, 2022.

[37] S. Fonna, I. Bin M. Ibrahim, Gunawarman, S. Huzni, M. Ikhsan, and S. Thalib, "Investigation of corrosion products formed on the surface of carbon steel exposed in Banda Aceh's atmosphere," Heliyon, vol. 7, no. 4, p. e06608, 2021.

[38] J. Shi, J. Ming, Y. Zhang, and J. Jiang, "Corrosion products and corrosion-induced cracks of low-alloy steel and low-carbon steel in concrete," Cem. Concr. Compos., vol. 88, pp. 121–129, 2018.

[39] Y. Wan et al., "Insight into atmospheric pitting corrosion of carbon steel via a dual-beam FIB/SEM system associated with high-resolution TEM," Corros. Sci., vol. 152, no. November 2018, pp. 226–233, 2019.

[40] I. B. Obot, A. A. Sorour, C. Verma, T. A. Al-Khaldi, and A. S. Rushaid, "Key parameters affecting sweet and sour corrosion: Impact on corrosion risk assessment and inhibition," Eng. Fail. Anal., vol. 145, p. 107008, Mar. 2023.

[41] R. De Motte et al., "A study by electrochemical impedance spectroscopy and surface analysis of corrosion product layers formed during CO2 corrosion of low alloy steel," Corros. Sci., vol. 172, no. February, p. 108666, 2020.

[42] E. S. D. De Oliveira, R. F. Da Costa Pereira, I. R. De Melo, M. A. G. De Andrade Lima, and S. L. U. Filho, "Corrosion behavior of API 5L X80 steel in the produced water of onshore oil recovery facilities," Mater. Res., vol. 20, pp. 432–439, 2017.

[43] A. Kahyarian, M. Achour, and S. Nesic, CO2 corrosion of mild steel. Elsevier Ltd, 2017.

[44] T. Yan, L. C. Xu, Z. X. Zeng, and W. G. Pan, "Mechanism and anti-corrosion measures of carbon dioxide corrosion in CCUS: A review," iScience, vol. 27, no. 1, p. 108594, 2024.

[45] D. Fonseca, M. R. Tagliari, W. C. Guaglianoni, S. M. Tamborim, and M. F. Borges, "Carbon Dioxide Corrosion Mechanisms: Historical Development and Key Parameters of CO2-H2O Systems," Int. J. Corros., vol. 2024, 2024.

[46] B. Janković, B. Adnađević, and J. Jovanović, "Application of model-fitting and model-free kinetics to the study of non-isothermal dehydration of equilibrium swollen poly (acrylic acid) hydrogel: Thermogravimetric analysis," Thermochim. Acta, vol. 452, no. 2, pp. 106–115, 2007.

[47] R. Rizzo, S. Baier, M. Rogowska, and R. Ambat, "An electrochemical and X-ray computed tomography investigation of the effect of temperature on CO2 corrosion of 1Cr carbon steel," Corros. Sci., vol. 166, p. 108471, Apr. 2020.

[48] A. Dugstad, "The Importance of FeCO3 Supersaturation on the CO2 Corrosion of Carbon Steels," CORROSION 1992. pp. 1–13, Apr. 27, 1992.

[49] K. Chokshi, W. Sun, and S. Nesic, "Iron Carbonate Scale Growth and the Effect of Inhibition in CO2 Corrosion of Mild Steel," CORROSION 2005. pp. 1–23, Apr. 03, 2005.